

CHARACTERIZATION OF TRANSVERSE CRACK AND CRACK GROWTH IN A RAILWAY RAIL

A. Hassani and R. Ravaee

ahasani@semnan.ac.ir

Date of Receive: February 2008 Date of Acceptance: May 2008

Department of Materials Science and Engineering, Faculty of Engineering, Semnan University, Semnan, Iran

Abstract: To ensure the rail transportations safety, evaluation of fatigue behavior of the rail steel is necessary. High cycle fatigue behaviour of a rail steel was the subject of investigation in this research using fracture mechanics. Finite element method (FEM) was used for analyzing the distribution of the stresses on the rail, exerted by the external load. FEM analysis showed that the maximum longitudinal stresses occurred on the railhead. To find out about the relation of crack growth with its critical size, and to estimate its lifetime, the behaviour of transverse cracks to rail direction was studied using damage tolerance concept. It revealed that transverse crack growth initially occurred slowly, but it accelerated once the crack size became larger. Residual service life was calculated for defective segments of the rails. In addition, allowable crack size for different non-destructive testing intervals was determined; the allowable crack size decreased as the NDT intervals increased.

Keywords: Rail, Critical Crack Size, Fracture Toughness, Fatigue Crack Growth, Finite Element Method.

1. INTRODUCTION

Crack geometry and stresses in the railhead are usually characterized by stress intensity factor, K , and resistance to fracture is described by fracture toughness, K_{IC} [1]. Fracture resistance in plane strain conditions, K_{IC} , is an indication of material resistance to crack propagation in a tensile loading. To obtain K_{IC} it is assumed that the crack tip plastic zone is small in comparison with the crack length and the specimen dimensions [2]. To evaluate the potential for unstable growth of cracks in head of the rail Grade 900A- UIC60, a probabilistic approach, based on fracture mechanics fundamentals, can be used. This approach combines the effects of stress, crack length, and material fracture resistance to establish a failure criterion. The criterion for failure embodied in this approach is stress intensity factor, K , assumed to be equal to the fracture toughness, K_{IC} of the material. Application of this approach requires a means of determining an analytical expression for the stress intensity factor that could be applied to various rails. Standard test techniques were used to measure fracture toughness, K_{IC} . Evaluation of critical crack size that triggers fracture under service condition plays a central role in

application of the theory. Besides, growth of fatigue crack must be analyzed to complete the knowledge on behavior of the cracked structures. Combined effects of load, stress distribution, fracture properties and crack growth characteristics, which can vary broadly in practice, must be considered. For determination of allowable crack sizes and for probabilistic calculations and a choice of suitable safety factors for sub-critical and critical crack propagation, an appropriate selection of crack sizes is necessary [1].

2. REVIEW OF RAIL FRACTURE ANALYSIS

2.1. Stresses and Loads

Fracture in rails is a relatively complicated problem. To study fracture, different conditions such as variable and complex loadings, secondary stresses, seasonal changes in environment conditions etc. must be taken into account. Rails are subjected to primary and secondary loading components. In primary loading, the wheel load is applied from rolling contact to the rail as bending stresses, axial stresses, and Hertzian pressure [3]. Bending stresses arise from the axle static load being

normally about 8 to 22.5 tones and the dynamic motions of vehicles (pitch, bounce and rocking) cause fluctuations in the magnitude of vertical wheel loads on the rail as trains travel over the track [1,3]. Maximum magnitude of these stresses depends upon the up and down movement of the sleepers, that is, upon the quality of the track substructure. Usually, different trains with different axle loads travel over the tracks. The rail weight itself may also contribute bending stresses. Defects in the running surface of the rails such as joints, dips and twists as well as irregularities in the wheel such as flats and out-of-roundness may play a role too [4]. Axial stresses arise from structural irregularities of the track and from the acceleration and deceleration of the train during train start and stop. The loading due to rolling contact plays a major role in the early crack extension stage. There is additional loading in lateral direction especially in curved track sections and at switches and crossovers. These forces are also dynamically magnified with increasing speed. The main load case for rails in switches is lateral bending [5]. Secondary loads including thermal and residual stresses are superimposed by primary loads. Axial thermal stresses, which are produced from intensive temperature fluctuations, are tensile stresses at lower temperatures; however, these stresses are compressive at higher temperatures. At temperatures about 0°C, high tensile thermal stresses are combined with relatively low toughness values of the rail materials, so, most rail failures occur at such temperatures [4]. Statistical analyses of rail failures have shown that temperature has a strong influence on the failure probability [6]. Residual stresses (tensile or compressive) in rails arise from the manufacturing processes (heat treatment and roller straightening), welding at rail joints or wheel-rail contact [5].

2.2. Crack Initiation and Propagation

Cracks may initiate at or below the surface due to high traction forces that are resulted from fast motion of vehicles over the track. Sub-surface cracks propagate towards the rail surface and behave like original surface cracks after penetration [7]. Crack initiation and propagation may be explained in following statement. A dark spot develops at the surface causing the crack to

occur at the surface or subsurface of the rail. Subsequently, the crack grows in an inclined angle below the surface and then it branches into a horizontal and a transverse crack at a certain point. The transverse crack extends down into the rail and finally causes its fracture [8]. Lubricants such as water play an important role in crack extension. Indeed, lubrication slows down crack nucleation but accelerates the subsequent crack growth. Among many distinct forms of crack, the two progressive transverse defects of detail fracture and tache ovale defect are known to be more important from fracture mechanics viewpoint [6]. The first type usually originates from a longitudinal seam or streak near the running surface on the gauge side of the railhead, but the second type originates from manufacturing defects, such as hydrogen flakes. In the present study the first type of the crack is focused. Fig. (1) shows the geometry of a transverse internal rail defect (such as a detail fracture), modeled as an elliptical flaw embedded in the railhead [9].



Fig. 1. Modeling of internal defect in railhead [9].

2.3. Critical Crack size

A critical crack size may be defined as the flaw size that can be expected to cause a failure under the critical load. On this basis, the critical load itself is defined as the load under which crack propagation just starts. Probabilistic fracture mechanics could be applied to estimate the cumulative probability distribution of critical crack sizes. For realistic assumptions, probabilistic calculations show a good agreement with practical experiences. But, the extreme calculation results are not realistic in every case. Appropriate selection of effective crack size resulting from the calculation is necessary.

3. EXPERIMENTAL

the crack length, a , must be larger than $2.5 \left(\frac{K_{IC}}{\sigma_{ys}} \right)^2$ according to BS 7448 [11], while w is

usually twice the size of thickness and the allowed range of w/B is 2-4. It should be noted that this standard is applicable only for determination of K_{IC} for the rail steels. The material used in this study was Grade 900A, UIC60 rail steel having the mechanical properties shown in Table (1) and the chemical composition in Table (2). Dimensional specifications of the rail are summarized in Table (3). There is no adapted equivalent for this steel in DIN standard, but it nearly is similar to AISI-1070 steel. Digit 900 represents tensile strength of 90 kg/mm².

A carbon content of 0.6 to 0.8 ensures yield strength, ultimate strength and hardness of the rail to increase [9]. The optimum Si content ranges from 0.2 to 0.3wt%, but presence of manganese in the range of 0.8-1.3wt% improves wear properties and, meanwhile, corrosion and oxidation resistance of the rail [9]. In addition, it is said [3,9] that the rail hardenability, when the composition is controlled correctly, increases such that it still has a good hardness after normalization. Microscopic observations have detected that the material has a very fine pearlitic microstructure with minimum sulphide inclusions and no ferrite in it [10].

To obtain reliable plane strain fracture toughness, K_{IC} , several tests should be carried out. Therefore, ten compact tension (CT) specimens were prepared from a UIC60 railhead steel using Electrical Discharge Machining (EDM). They were cut from centric part of the railhead normal to the rail cross section, machined and then notched to the standard dimensions. The specimen geometry including the notch configuration is given in Fig. (2). Both the specimen thickness, B , and The tests that

were performed utilizing an Instron-8502 test machine consisted of two parts:

1- Applying a cyclic force to the specimen for a fatigue pre-crack to be made at the tip of the notch that had been machined while preparing the specimen. The size of this pre-crack and the amount of the applied oscillating force were calculated in accordance with ASTM E399-83 [12] and BS 7448 [11]. The fatigue pre-crack was made at room temperature but all other conditions were considered to be just the same as fracture test. For the fatigue crack initiates as quickly as possible, *chevron* type notch was machined in the specimen. The chevron notch shape is illustrated in Fig. (3) [12] and the place where the specimen must be removed from the railhead is shown in Fig. (4).



Fig. 2. The specimen geometry[11].



Fig. 3. The Chevron Notch [12].

Table 1. Mechanical properties of the rail Grade 900A.

Tensile Strength (MPa)	Yield Strength (MPa)	Elongation (%)	Hardness (BHN)
880	410	10	240-250

Table 2. Chemical composition of the material(wt.%).

Element	C	Mn	Si	Fe
wt%	0.6-0.8	0.8-1.3	0.1-0.5	balance

Table 3. Dimensions of the rail, UIC60.

Weight per meter length (Kg)	Height (mm)	Bottom Width (mm)	Head Width (mm)	Web Thickness (mm)
60.340	172	150	74.3	16.5



Fig. 4. The place where a sample was removed [13].

2- Applying an increasing force to the pre-cracked specimen until it fails. According to the recommended procedure described in ORE D156 [13], the tests were performed at temperature of -20°C ($\pm 2^{\circ}\text{C}$) to improve possibility of measuring valid fracture toughness. It should be noted that, in general, fracture toughness decreases with decreasing temperature. So, the less the test temperature is, the more valid fracture toughness will be obtained [13]. The fracture surfaces were examined using a Philips XLC SEM at 20 kV and typical micrographs revealing the fracture surface morphology were taken.

4. RESULTS AND DISCUSSION

4.1. Study of Fracture Surfaces

Macroscopic observations of fracture surfaces of the specimens clearly indicated two discrete zones. These two distinct zones are shown in the optical micrograph (a) in Figs.(5). The boundary of these zones is well distinguished. One zone with a shiny appearance is indicative of gradual crack propagation due to fatigue development during the cyclic loading, while the other with an opaque dark look shows that crack propagation has happened after fatigue crack length reached a critical size in non-cyclic loading. The fatigue fracture surface appears to be even, smooth and shiny with no trace of plastic deformation in it. The fracture surface of the critical region looks rough with "shear lips", which is associated with forced ductile fracture, indicating that plane strain conditions occurred. SEM fractographs, (Figs. 5 (b, c and d)), show entirely different morphologies for the two zones of fatigue fracture and final fracture on the fracture surface of the sample.

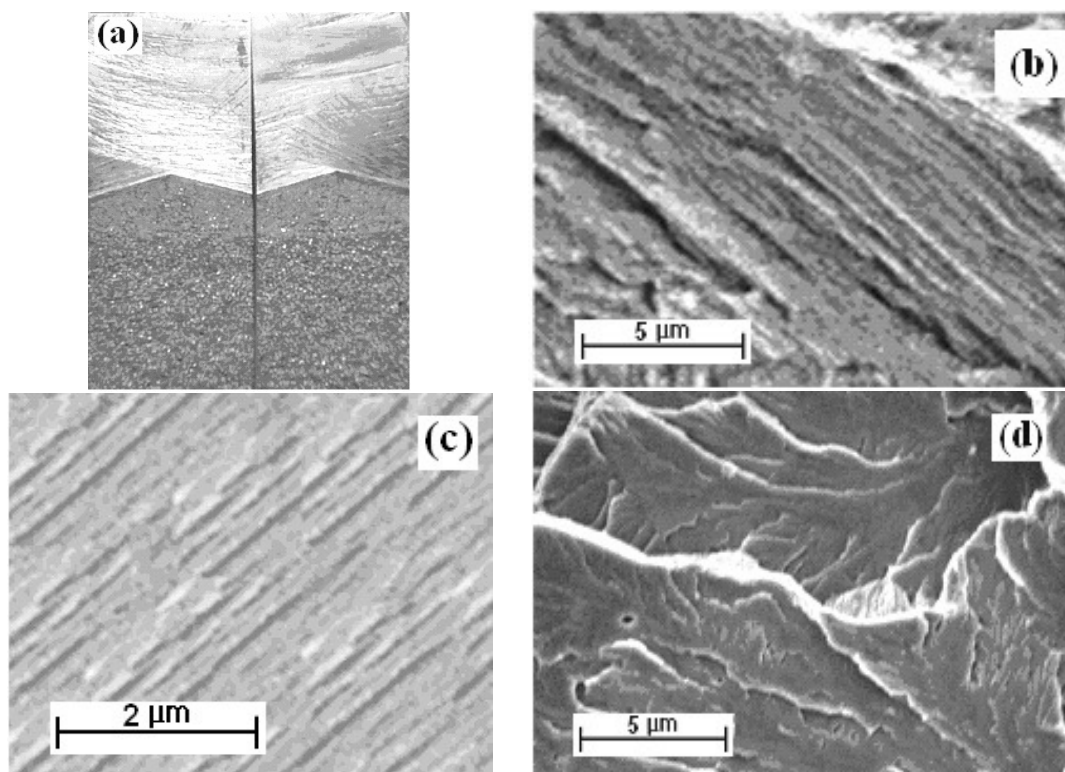


Fig. 5. (a) Optical micrograph of fracture surface of a specimen. (b), (c) and (d) SEM Fracture surface morphologies: (b) and (c) fatigue fracture surface showing the presence of striations; (d) final forced sheared fracture surface due to plane strain conditions.

Figs. (5-b) and (5-c) clearly reveal the presence of many small parallel lines, referred to as fatigue striations which may appear on fatigue fracture surface in many materials and are oriented parallel to the advancing crack front. Forsyth and Ryder [14] provided critical evidence that each striation represents the incremental advance of the crack front as a result of one loading cycle and that extent of this advance varies with the stress range. This is shown clearly in Fig. (5-b), which reveals striations of differing width that results from a random loading pattern, as explained previously. Indeed, striations are most clearly observed on flat surfaces associated with plane strain conditions. In Fig. (5-d) the final fracture zone is illustrated in which the coarse steps and deep river patterns (associated with the 3-D tensile stresses, plane strain conditions and forced ductile fracture in low temperatures) are apparent.

4.2. Plane Strain Fracture Toughness Test

According to BS 7448, the maximum force for creation of the fatigue crack (F_f) in the final length of 1.3mm or at 50% of the final crack propagation must be less than

$$F_f = \frac{0.2B(w-a)^2(\sigma_{YSP} + \sigma_{TSP})}{(2w+a)}, \text{ where } \sigma_{TSP} \text{ and}$$

σ_{YSP} are the tensile strength at the temperature of fatigue test and the yield strength at the temperature of fracture test respectively.

The value of $F_f = 24.2$ kN was obtained from above equation for the rail specimen. For easily controlling the crack size, however, it would be better to take the maximum value of the oscillating force equal to 12 kN. So, if

$$R = \frac{F_{\min}}{F_{\max}} = \frac{\sigma_{\min}}{\sigma_{\max}} = 0.1 \text{ (in cyclic loading of the}$$

specimen this ratio range is -1 to +0.1), the minimum value of the oscillating force would be 1.2. The value of a must range between $0.45w$ and $0.55w$. After calculating a value, this value was marked at the tip of the notch to specify maximum pre-crack length that was to be made. The optimum frequency for the cyclic force was determined to be 15Hz.

Data related to the fatigue crack creation are summarized in Table (4). The value of K_{IC} emanated from a crack with blunt tip is larger than that obtained from a sharp tip crack.

Therefore, to ensure that the crack tip was sharp enough, it was necessary that K_{\max} in cyclic loading to be less than $0.6K_{IC}$. On this basis, maximum and minimum values of the applied oscillating force decreased to 0.6kN and 6kN respectively, while the frequency was chosen 25Hz.

Table 4. Data related to the fatigue crack creation.

Specimen No.	$F_{\max}=12\text{kN}$ $F_{\min}=1.2\text{kN}$ Freq=15Hz	$F_{\max}=6\text{kN}$ $F_{\min}=0.6\text{kN}$ Freq=25Hz	K_{\max} ($\text{MPa}\sqrt{m}$)
	Cycle	Cycle	
1	128000	25000	15.2
2	115000	25000	14
3	116000	25000	14.7
4	123000	25000	14.8
5	118000	25000	15.1
6	126000	25000	15.0
7	117000	25000	14.6
8	122000	25000	14.9
9	119000	25000	15.1
10	121000	25000	14.3

The stress intensity factor, K , in CT specimens was calculated using following empirical relationship [12]:

$$K = \frac{P \left\{ (2 + a/w) [0.886 + 4.64(a/w) - 13.32(a/w)^2 + 14.72(a/w)^3 - 5.6(a/w)^4] \right\}}{B\sqrt{w}(1-a/w)^{3/2}} \quad (1)$$

This relationship can be applied in the range of

$0.2 < \frac{a}{w} < 1$ with error of less than 5% [12]. A

summary of K_{IC} test results at -20°C is given in Table (5). In addition, a typical load-displacement record obtained during one of those tests is shown in Fig. (6). All the values are valid according to the measures proposed by ORE D156 [13].

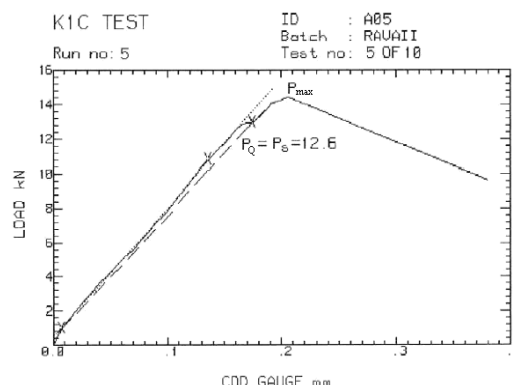


Fig. 6. A typical load-displacement record obtained during K_{IC} testing.

Table 5. Summary of K_{IC} test results

Test No	K_{IC} (MPa \sqrt{m})
1	32.4
2	28.9
3	30.2
4	28.8
5	31.3
6	29.4
7	30.9
8	32.1
9	28.5
10	31.7
Ave	30.4

The criterion for minimum thickness in E399

test which is expressed as $B_{min} = 2.5 \left(\frac{K_{IC}}{\sigma_{ys}} \right)^2$ is

based on the experimental work carried out by many authors [e.g.:8, 11,12] on steel and aluminum alloys. If the specimen thickness and/or the crack length are smaller than those proposed in the criterion, the resulted K_Q will be larger than K_{IC} . Consideration of the data emanated from the tests that are tabulated in Table (6) reveals that the criterion for the minimum thickness and crack length in the tests carried out in present study is about 8 mm. A comparison of this value with the specimen thickness and its fatigue crack length indicates that the mean K_{IC} obtained from these tests are valid and reliable.

4.3. Critical Crack Size and Crack Growth Characterization

Critical crack size for detail fracture was calculated from the formula [9]:

$$K_{IC} = \frac{2}{\pi} M_S M_1 \sigma \sqrt{\pi a_c} \quad (2)$$

where a_c is the semi-major axis critical length of the elliptical crack, M_S is an empirical factor to account for the elliptical shape of defect, M_1 is an empirical factor to account for the finite dimensions of the rail cross section and σ is the longitudinal stress. A summary of critical crack size calculation results is given in Table (7).

As seen, critical crack size depends only upon the value of a , therefore, the value of b is assumed to be equal to the value of a in subsequent calculations. The number of cycles, N , to grow a crack from an initial size, a_i , to a larger size, a_f , can be calculated from the following equation [11]:

$$N = \frac{1}{C} \int_{a_i}^{a_f} \frac{(1 - R(a))^q}{(G(a) \Delta \sigma(a) \sqrt{\pi a})^p} da \quad (3)$$

where a is characteristic defect size, R is the minimum to maximum stress ratio, $G(a)$ refers to a geometry function that depends on the type of defect which appears as $G(a) = 2M_S M_1(a)/\pi$ for the detail fracture, $\Delta \sigma$ is the stress range and the material constants C , p and q have experimentally been determined elsewhere [15]. Above equation is derived originally from Paris equation,

$$\frac{da}{dN} = C \frac{\Delta K^p}{(1 - R)^q} \quad (4)$$

by treating it as a separable ordinary differential equation. In this equation, ΔK is stress intensity factor range. In general, the stress range $\Delta \sigma$, the stress ratio R and the geometry function $G(a)$ depend on the crack size [15].

Table 6. Results of K_{IC} test ($w=40\text{mm}$ and $B=20\text{mm}$ and σ_Y^* is the yield stress at the test temperature).

No.	1	2	3	4	5	6	7	8	9	10
Quality										
a(mm)	19.9	19.5	19.7	19.5	19.8	19.6	19.8	19.9	19.6	19.4
P_{max} (kN)	13.7	14.4	13.9	13.2	14.7	14.3	13.9	14.7	13.9	13.8
P_Q (kN)	12.8	12.4	12.2	12.5	12.6	12.4	12.7	12.3	12.7	12.8
P_{max}/P_Q	1.07	1.16	1.13	1.05	1.16	1.15	1.09	1.19	1.1	1.08
K_Q (MPa \sqrt{m})	32.4	28.9	30.2	28.8	31.3	29.4	30.9	32.1	28.5	31.7
K_{IC} (MPa \sqrt{m})	32.4	28.9	30.2	28.8	31.3	29.4	30.9	32.1	28.5	31.7
σ_Y^* (MPa)	581	581	581	581	581	581	581	581	581	581
$2500 (K_Q / \sigma_Y^*)^2$	7.77	6.18	6.75	6.14	8.41	6.4	7.07	7.63	6.01	7.44

Table 7. Critical crack size.

K ($\text{MPa}\sqrt{\text{m}}$)	a (mm)	b (mm)
28.4 to 30.3	5	1 to 19

The crack growth from an initial size of a_i to a service limit size of a_f is simulated by determination of relevant load cycles, N [16]. In this simulation, influences due to rail temperatures, neutral temperatures, residual and bending stresses were assumed to be random values. Residual cycles of rail life versus initial crack size are shown in Fig. (7). The figure indicates that growth rate of rail defects is relatively slow at first, but it increases as the flaw becomes larger. Transverse cracks in the railhead extend in the critical state frequently up to the running surface of the rail. This is independent of the crack origin in the head [17]. Displayed graphically in Fig. (8) are the allowable crack size \bar{a} versus the non-destructive testing intervals for transverse cracks for different traffic conditions. As it is to be expected, allowable crack size decreased with increasing the testing intervals. The service limit of the transverse crack on the railhead was about 5 mm.

4.4. Finite Element Method Analysis

To model the rail profiles for the purpose of analyzing the stresses, the ANSYS software was used. For the analysis implementation, a rail of UIC60 profile with 5-meter length was modeled. The cause for choosing such a length was that the nine sleepers could be placed underneath the rail at the standard distances. Since the rail cross section was asymmetric and irregular, the elements used for automatic mesh generation in the profile were selected to be the two dimensional triangle elements, called PLANE-2, each had 6 nodes amidst their sides and at their corners. For the regular surfaces with straight lines, however, one could use elements with fewer nodes or even rectangular elements. Transformation of the surface grids to the spatial ones was made by the three-dimensional 8-node linear brick elements, called SOLID 45. It was necessary that the three-dimensional FE grids to be matched along the depth (Figs. (9)). The modulus of elasticity of the rail steel was taken 200 GPa with the material density of 7800 kg/m^3 and the Poisson's ratio of 0.3. To model the pad, the elements COMBIN 14, each composed of a spring with stiffness factor of $k=3032 \times 10^6 \text{ N/m}$

and a damper with damping coefficient of $C_V=29 \times 10^3 \text{ N.s/m}$, were used. The nine wooden sleepers were used in the analysis; each had 20 cm width and 100 kg mass. The axis-to-axis interval of sleepers was 60 cm. Considering high axial stiffness of the sleeper and its noticeable mass, the sleeper was modeled as a concentrated mass in this analysis. Since one rail was modeled only, half weight of the sleeper, i.e. 50 kg, was considered as the concentrated mass under the pad element and over the ballast element. It must be noted that, because of symmetry with respect to the line center, the internal forces had no effects in the normal direction.

**Fig. 7.** Residual cycles of rail life versus initial crack size.**Fig. 8.** Allowable crack size of transverse cracks depending on non-destructive testing intervals for different traffic conditions.



Fig. 9. (a) two dimensional FE mesh of the rail cross section and (b) three-dimensional FE mesh of the rail.

For modeling of the ballast the elements COMBIN 14 were also used for which the constants in the analysis were $k=8 \times 10^6$ N/m and $C_V=15 \times 10^3$ N.s/m. On this basis, the schematic plan of the model can be drawn as in Fig. (10).

As seen in Fig. (9-b), for modeling the pad, the sleeper and the ballast below it 18 parallel elements of MASS and COMBIN 14 were used. In this case, the values of k and C_V for the elements COMBIN, and the mass value for the elements MASS were obtained by dividing above values by number 18 [18]. The axial load, taking the rail traffics conditions in Iran into account, was chosen 250 kN. The load for each wheel was then taken to be 125 kN. In primary models, only one normal load of 125 kN has been used but, in more advanced models a lateral load, which was applied on the worn side of the railhead in a height of 15 mm or more from the upper surface of the railhead, was also utilized. The normal load was applied at the midpoint between the forth and the fifth sleepers. The amount of lateral force depends on parameters like arc radius, number of cycles, normal load, type of coach used and the train velocity among which the arc radius and the velocity must be accounted the main parameters.

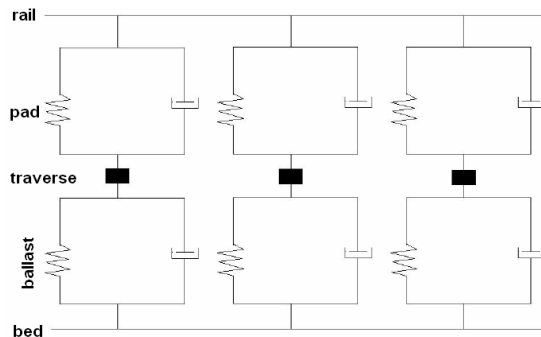


Fig. 10. Schematic of the model components.

For low velocities and large radii the lower L/V ratios and for high velocities and small radii the higher L/V ratios were used, where L is the lateral force and V is the normal force. In this analysis the ratio $L/V=0.2$ can be used for the lateral load determination [18]. After making the model and loading that, static analysis of the stresses was performed by ANSYS; the results are illustrated in Figs. (11). The problem was considered in the following statement. The normal force exerted from the wheel on the rail was considered to be in equilibrium with the extended load applied from the rail bed causing bending moment in the rail to occur. At points where bending moment along the rail was positive, compressive stresses occurred at the top of the railhead. On the contrary, at points where the bending moment was negative, tensile stresses occurred at the top of the railhead. This is shown in Fig. (11-a) in which the longitudinal stresses created at the top of the railhead had maximum value of -118 MPa. The neutral axis occurs at the rail web upon which the compressive and tensile stresses neutralize each other, so, the amount of longitudinal stresses on this axis is zero. In the rail UIC60 the height was 17.198cm and the height of the neutral axis was 8.09cm. Hence, the maximum space between the railhead and the neutral axis was $C=9.108$ cm. So, maximum tensile residual stress occurred at 5 mm below the railhead surface and the stress arisen out of the bending moment was obtained at $Z= 8.608$ mm. It can also be seen in Fig. (11-a) that the amount of the stress at this point is approximately -103 MPa. Tensile stresses also occurred in the rail base with an approximate amount of 20 MPa. Fig. (11-b) shows the stress values in y-direction where the stress values were less than those in z-direction.

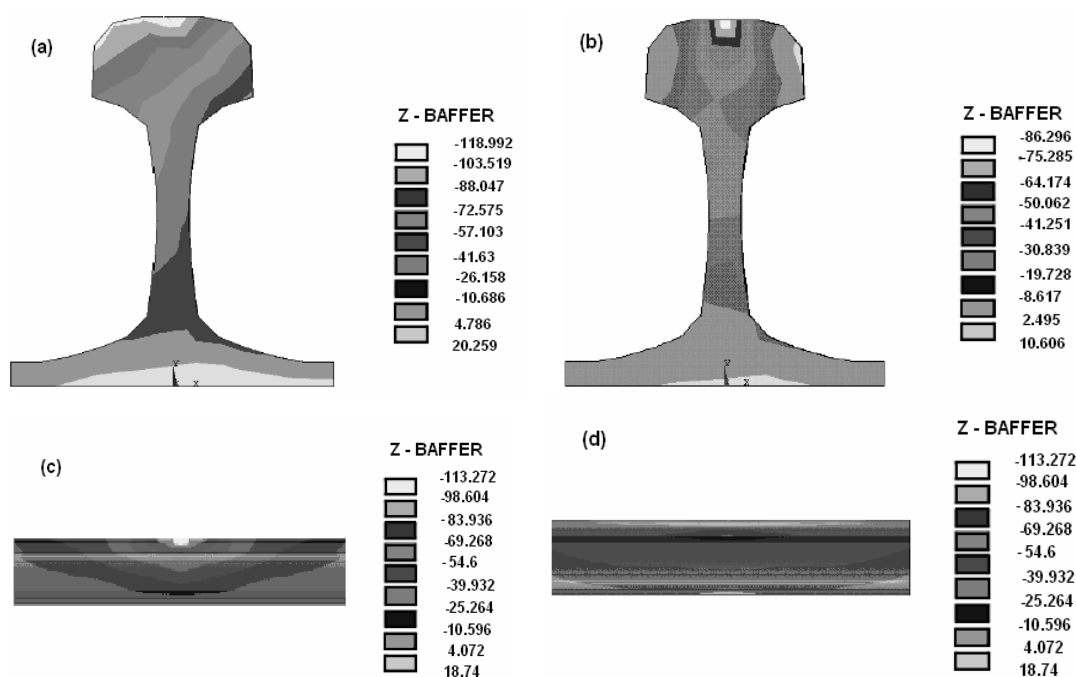


Fig. 11. Distribution of longitudinal stresses: (a) in the rail cross section and the place where normal and lateral forces are applied. (b) in y-direction in the rail cross section and the place where normal and lateral forces are applied. (c) in the rail surface and the side where lateral forces are applied. (d) in the rail surface and the other side of it.

Therefore, these stresses play a less important role in crack propagation, and for the fracture evaluation, it is necessary to focus on the cracks having perpendicular direction to the longitudinal stress. Figs. (11-c) and (11-d) show distribution of the longitudinal stresses on the surfaces of both sides of the rail piece. Considering these figures reveals that getting away from the place where the wheel force applies to the rail, and getting closer to the sleepers located in both sides of the wheel, one can say that the compressive longitudinal stresses in the railhead changed to the tensile ones. The force applied to the rail from the wheel reached its equilibrium value by the sleepers and the rail bed causing a negative bending moment over the sleepers, caused the tensile longitudinal stresses to occur. It is clearly seen that there is a good agreement between the results obtained from mathematical analysis and the results obtained from the finite element method.

5. CONCLUSIONS

In order to define the allowable crack size in this

research, fatigue behaviour of transverse cracks in the railhead was studied. For the purpose of analyzing the stresses exerted to the rail, FEM was used, and CT was performed on the rail steel to obtain K_{IC} value. By applying the fracture mechanics relationships, the following results were obtained:

1. From the FEM analysis one can appreciate that the maximum longitudinal stresses occurred on the railhead.
2. The critical size of transverse cracks in the railhead was approximately 10mm at temperature of -20°C .
3. Transverse crack growth in the railhead initially occurred slowly, but it accelerated once the crack size became larger.

The allowable crack size depended on the NDT intervals; it decreased as the NDT intervals increased.

REFERENCE

1. P. Andrew, T. Kim Parnell, D. Caligiuri, A. Sire, "Rail Cracking due to Residual Stress from Manufacturing and Heat Treating", Parnell Engineering & Consulting, p. 13,

- 2003-2004.
2. S. Beretta, M. Boniardi, M. Carboni, H. Desimone, *Engineering Failure Analysis*, 12 p.157–165, 2005.
3. D. Y. Jeong, *Progress in Rail Integrity Research*, U. S. Department of Transportation Research and Special Programs Administration, Cambridge, Massachusetts, p. 17, 2001.
4. A. Skyttebol, B.L. Josefson, J.W. Ringsberg, *Engineering Fracture Mechanics*, 72, p.271–285, 2005.
5. U. Zerbst, K. Madler, H. Hintze, *"Engineering Fracture Mechanics"*, 72, p.163–194, 2005.
6. K. O. Edel, *Theoret. Appl. Fracture Mech.*, 9, p. 75-82, 1988
7. K. L. Johnson, "The strength of surfaces in rolling contact." *Proc. Inst Mech Engng*, 203, p. 151–163, 1989.
8. M. Ishida, N. Abe "Experimental study on rolling contact fatigue from the aspect of residual stress", *Wear*, 191, p. 65–71, 1996.
9. D. Y. Jeong, "Correlations Between Rail Defect Growth Data and Engineering Analyses, Part I: Laboratory Tests", U.S. Department of Transportation Research and Special Programs Administration, Cambridge, Massachusetts, P. 10,19, 2003.
10. Technical Specification For the Supply of Rail UIC 860, p. 78, 1986.
11. Fracture mechanics toughness tests, BS 7448.
12. Standard Test Method for Plane Strain Fracture Toughness (K_{IC}) of Metallic Materials, ASTM E 399-83.
13. Recommended procedure for the determination of the plane strain fracture toughness (K_{IC}) of rail steels, ORE report 3, 1987.
14. P. J. Forsyth, D. A. Ryder, *Metallurgica*, 63, p. 117, 1961.
15. D. Y. Jeong, "Correlations Between Rail Defect Growth Data and Engineering Analyses, Part II: Field Tests", U.S. Department of Transportation Research and Special Programs Administration, Cambridge, Massachusetts, P. 19, 2003.
16. K. O. Edel, *Theoret. Appl. Fracture Mech.*, 4, p. 109-116, 1987.
17. J. J. Scutti, R. M. Pelloux, and R. F. Moleno: "Fatigue behavior of a rail steel," *Fatigue & Fracture of Engineering Materials & Structures* 7, p. 121-135, 1984.
18. Z. Wen, X. Jin, W. Zhang, "Contact-impact stress analysis of rail joint region using the dynamic finite element method", *Wear*, 258, p. 1301-1309, 2005.